Selecting an optimal configuration for the Soil Moisture and Ocean Salinity mission

Philippe Waldteufel,[1] Jacqueline Boutin,[2] and Yann Kerr[3]

Received 9 July 2002; revised 11 August 2002; accepted 14 November 2002; published 25 March 2003.

[1] The Soil Moisture and Ocean Salinity (SMOS) mission is aimed at monitoring, globally, surface soil moisture and sea surface salinity from radiometric L-band observations. The SMOS radiometer relies upon a two-dimensional (2-D) synthetic aperture concept in order to achieve satisfactory spatial resolution performances for a minimal cost in terms of payload mass and volume. Counterparts of this advantage are reduced radiometric sensitivity and increased complexity. The performances expected from SMOS, in terms of measurement accuracy, spatial resolution, and revisit time, depend on many parameters, among which several are crucial for assessing the payload and mission configurations. Most prominent among those configuration parameters are the flight altitude, the length of the interferometer arms, the spacing between radiating elements, and the tilt angle of the antenna plane. Their selection has to be optimized, so as to satisfy both scientific requirements and main technical constraints. This paper describes the way the optimization was carried out during the SMOS phase A. After assessing the main drivers on instrument configuration from the science requirements, the goal was to find an optimal trade-off, minimizing technical challenges while fulfilling the science objectives. It was found that, even though salinity retrievals are the most challenging, soil moisture retrievals were the most demanding in terms of mission definition and that a configuration exists to satisfy the required retrieval accuracies. The obtained configuration was then checked against ocean salinity retrievals and found satisfactory. *INDEX TERMS:* 4275 Oceanography: General: Remote sensing and electromagnetic processes (0689); 1866 Hydrology: Soil moisture; 4283 Oceanography: General: Water masses; 0694 Electromagnetics: Instrumentation and techniques; *KEYWORDS:* radiometry, interferometry, optimization, soil moisture, salinity

Citation: Waldteufel, P., J. Boutin, and Y. Kerr, Selecting an optimal configuration for the Soil Moisture and Ocean Salinity mission, *Radio Sci.*, *38*(3), 8051, doi:10.1029/2002RS002744, 2003.

1. Introduction

1.1. SMOS Mission Objectives

[2] Soil Moisture and Ocean Salinity (SMOS) is a mission submitted to the European Space Agency (ESA) in answer to the 1998 call for Opportunity Missions in the framework of the Earth Explorer Programme [*Kerr*, 1998]. The project was selected for an extended phase A, and the phase B started mid-2002, aiming at a launch in 2006 [*Silvestrin et al.*, 2001].

[3] SMOS aims at monitoring on the global scale two quantities: surface soil moisture (SM) over land and surface salinity (OS) over the ocean. Both SM and OS are of major interest for climatic and meteorological studies. In addition, knowing surface soil moisture is important for hydrology, as well as for several applied aspects that concern water resources management. The SM and OS combination is made possible, as the same region (decimetric wavelengths) of the electromagnetic spectrum is particularly sensitive to these two variables [*Kerr et al.*, 2001].

[4] The requirements to fulfill the science objectives are as follows: (1) global SM estimates with a ground resolution of 50 km or better, maximum revisit of 3 days (at the equator and for morning passes only), and an accuracy of 4% volume [*Calvet et al.*, 1998; *Global Energy and Water Cycle Experiment/Biospheric Aspects of the Hydrological Cycle (GEXEW/BAHC)*, 2000; *Jackson et al.*, 1999; *Jackson and the Soil Moisture Mission*

[1]Institut Pierre Simon Laplace, Service d'Aéronomie, Verrières le Buisson Cedex, France.
[2]Institut Pierre Simon Laplace, Laboratoire d'Océanographie, Dynamique et de Climatologie, Paris, France.
[3]Centre d'Etudes Spatiales de la Biosphère, Toulouse, France.

0048-6604/03/2002RS002744

Working Group, 2002], (2) OS with a resolution of 200 km, over 10 days and with an accuracy of 0.1 on the practical salinity scale (PSS) which corresponds to parts per thousand (see GODAE).

[5] SMOS is thus a mission with fully fledged scientific objectives. However, being a small satellite with limited cost, its performances are not necessarily those ultimately wished for by the users' community. SMOS is therefore also meant to be a demonstrator aimed at paving the way for future, more ambitious missions.

1.2. Measurement Principle

[6] Retrieving SM and OS from space observations requires an instrument measuring directly the variables with the largest possible sensitivity and minimal perturbation so as to provide significant, global, and frequent measurements. Such requirements lead to using microwaves at low frequencies [*Swift and McIntosh*, 1983; *Schmugge and Jackson*, 1994]. As the signal produced by active techniques strongly depends on surface roughness properties, it is recognized that radiometry offers the most promising prospect [*Wigneron et al.*, 1999].

[7] In radiometry, the spatial resolution at ground level becomes a major technical issue since the longer the wavelength, the larger the antenna required for achieving a given spatial resolution. For this reason among others, it is not practical to use frequencies lower than 1 GHz. Such a requirement leads to selecting in the L band the 1.400–1.427 GHz frequency range, as it is protected for radio astronomical purposes.

[8] A spaceborne radiometer detects signals that are linked to the polarization dependent brightness temperatures (T_B) of the thermal power radiated by the surface. In turn, these temperatures depend on either SM or OS through their influence on surface emissivities.

[9] Over land surfaces, the emissivities strongly depend on SM [*Schmugge*, 1998]. In addition to some dependency on various soil parameters and surface temperature, an important factor is the effect of vegetation cover, which may in a first approximation be characterized by an optical thickness. Over the ocean, the dependency of the radiated temperature upon OS is weak, since its variation is only a few Kelvin for the entire range of open sea salinities. The sea surface temperature is an important factor, while the effect of sea state is very significant and still imperfectly assessed.

[10] While the theories of measurement still require further developments, the feasibility of SM and OS retrievals has been proven in many cases using ground and air borne experiments [*Chanzy et al.*, 1997; *Jackson et al.*, 1995; *Lagerloef et al.*, 1995; *Wilson et al.*, 2001]. So as to apply such results to a spaceborne instrument, the issue of spatial resolution, hence of the antenna size, becomes a central one. In this respect, the SMOS project is built around a two-dimensional synthetic aperture concept, derived from radio astronomy. It consists in using a synthesized antenna, i.e., an antenna that encompasses a large area while having restricted dimensions. With the design selected for SMOS, the payload becomes much lighter and easy to deploy than for a full, real antenna, making it a viable solution for small satellite opportunity missions.

[11] There are counterparts to this advantage. The instrument is innovative and thus without heritage; the post processing has to include a sophisticated image reconstruction step. Since reconstructed brightness temperatures are linear combinations of many correlation products, the resulting radiometric uncertainty is much larger than the figure obtained with a real antenna. In order to make up for this deterioration, all information obtained in the two-dimensional field of view should be used.

1.3. Optimization Problem and Approach

[12] During the SMOS instrument concept studies, it was necessary to find the best trade off between various and somewhat antagonistic constraints: accommodation on a small satellite bus, scientific requirements, instrument feasibility and performances. So as to find the optimal configuration two factors must be taken into account: (1) for a limited number of key design parameters, there is no straightforward way of selecting the best choice with respect to science requirements; (2) as the design parameters are interrelated, the best choice should be found in terms of the whole set of parameters rather than for each one separately. In other words, there is a need for a systematic search of an optimal configuration through a sort of parametric analysis.

[13] Describing this search and presenting its outcome are the purposes of this paper. We will present first the way SMOS operates and the relevant instrument parameters and constraints in relation with the corresponding scientific performances. Then we are faced with a somewhat paradoxical situation: while measuring sea surface salinity is a major objective of the mission and by far the most difficult to achieve, it was found that SM was the retrieved variable having the biggest influence on mission characteristics. So the optimization consisted in finding the configuration fulfilling the science objectives for SM. After describing the rationale and results thus obtained, we will report the validation of the found configuration for ocean surfaces.

2. Description of the SMOS Concept

2.1. Reconstructed Brightness Temperature Fields

[14] The SMOS interferometer consists of a planar, Y shaped structure; this shape was selected in order to

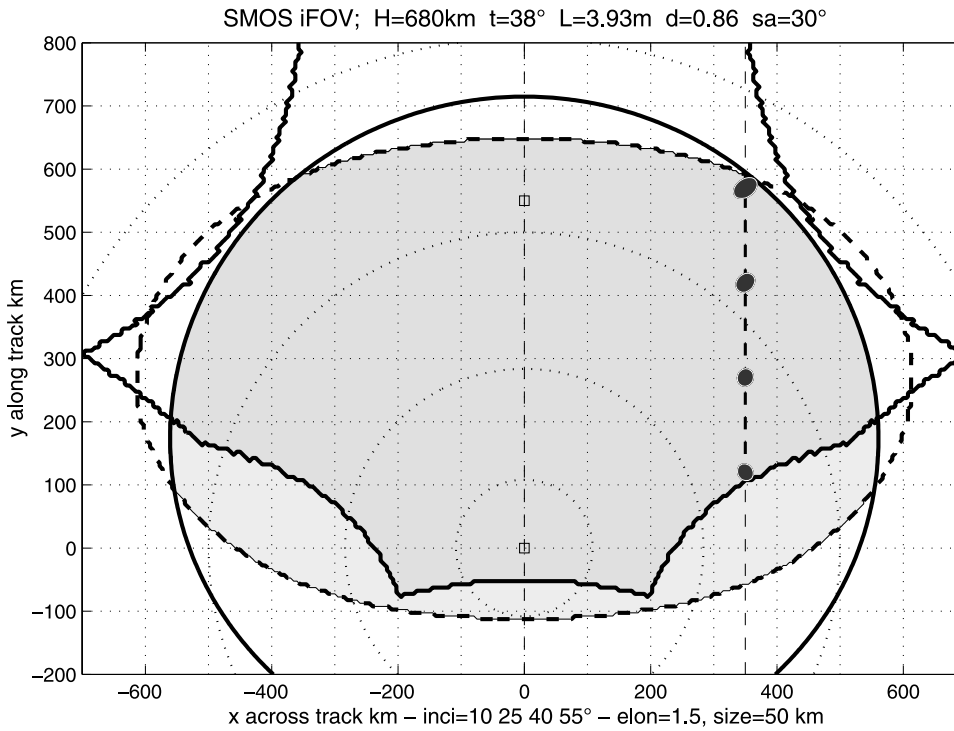

Figure 1. Example of the SMOS instantaneous FOV, when mapped on a geographical grid on Earth surface. The diagram is symmetrical with respect to the satellite track. Shown are the boundaries of the available zone for reconstructed brightness temperatures (thick black). Most of them are parts of ellipses, which correspond to replicated contours of Earth's horizon. Far on each side, straight-line segments indicate boundaries of the reconstruction zone. Also shown are spatial resolution limits (thick red line for pixel equivalent diameter s; thin red line for elongation e), contours of equal incidence angle (dotted blue; values 10, 25, 40, 55°), subsatellite point and intersection of antenna axis with Earth (squares), and a particular dwell line (green), 350 km away from ground track, along which samples of pixels are displayed. See color version of this figure at back of this issue.

minimize the relative number of redundant baselines. The independent baselines then fill a star-shaped domain as described by *Kerr et al.* [2000] and *Waldteufel et al.* [2000]. Each interferometer element consists of a broad beam antenna and a receiving channel. Voltages collected for each linear polarization are used to build complex correlation products, from which are derived the complex visibility functions for each baseline vector defined by a couple of elements.

[15] From the array of visibilities, 2-D fields of brightness temperatures are reconstructed in an angular frame of reference linked to the antenna plane. The reconstruction operator is basically a 2-D inverse Fourier transform. It is actually complicated by fringe washing phenomena. Fringe washing describes a worsening in spatial resolution caused by decorrelation of the target signal due to the finite receiver bandwidth as the synthetic beam is steered away from boresight [*Fischman et al.*, 2002]. Another complicating factor is the necessity to correct for differences in the patterns of interferometric radiating elements, as well as for misalignments in receiving channels and relative phases.

[16] The 2-D Field of View (FOV) of SMOS, translated into the geographical reference frame, is illustrated by Figure 1 for representative configuration parameters. The FOV is first restricted to the zone where temperatures can be reconstructed, accounting for the finite extent of the baseline domain where interferometric products are available. Moreover, the FOV is bounded by replicated scenes (aliases), owing to the fact that the spacing ratio $d = D/\lambda$ between interferometer elements, D being the antenna spacing and λ the wavelength, is chosen larger than would be required by the Nyquist criterion, mostly for engineering reasons indicated hereafter in section 3.1. The usable part of the FOV may, however, be extended to include zones where only sky signals are folded back, since such signals are very

weak and can be corrected. Then the FOV is mainly bounded by contours of replicated images of Earth horizon.

2.2. Retrieval of Geophysical Quantities

[17] For each integration time, of the order of a few seconds, the sensor images the whole FOV and hence all the pixels are acquired with varying view angles. As the satellite moves, a series of brightness temperature data is thus acquired and any given area on Earth is observed in successive locations within the FOV, along the so-called "dwell line," parallel to the satellite track.

[18] A significant point to be noted on Figure 1 is that dwell lines cross the contours of constant incidence angles α; in other words, SMOS provides brightness temperatures for a range of incidence angles, which is obviously larger as one comes nearer to the subsatellite track.

[19] Since emissivities depend both on surface geophysical characteristics and the incidence angle α, the principle of retrieval relies on finding the parameters which yield the best fit between theoretical simulations and measured multi angular brightness temperatures.

[20] Let $F(\alpha, p_i \ldots)$ be the direct (forward) model for a brightness temperature at the antenna level; F depends on the incidence angle α and on physical parameters p_i. A Bayesian approach allows taking advantage of a priori information available on the physical parameters. Then the retrieved p values are those which minimize the cost function C:

$$C = \sum_m \frac{[A_m - F(\alpha_m, p_i..)]^2}{\sigma_m^2} + \sum_i \frac{[p_i - p_{i0}]^2}{\sigma_{i0}^2}, \quad (1)$$

where the A_m are measured values with variances σ_m^2, and the p_{i0} are a priori estimates of the physical parameters, with a priori variances σ_{i0}^2. For example, in the ocean case, the second term in the r.h.s. of equation (1) accounts for auxiliary information about the sea surface temperature and the wind magnitude. The method used in the present study provides variance estimates σ_{xi}^2 affecting retrieved parameters, for each abscissa x across the FOV (see Appendix A).

[21] It is very likely that when SMOS is in operation it will be possible and necessary to improve direct models, even if only with semiempirical corrections derived from actual measurements. We nevertheless reckon that this should not modify significantly the results presented below, as the sensitivity of brightness temperatures to geophysical parameters is not likely to change drastically.

[22] The first term in the r.h.s. of equation (1) includes a summation over every incidence angle and every measured brightness temperature. Although the basic option retained for SMOS is dual polarization, the instrument has full polarimetric capability, i.e., the visibilities recorded by the interferometric radiometer allow to reconstruct the fields of all four Stokes parameters of the radiation collected by the antenna [*Martin-Neira and Garcia*, 1999; *Martin-Neira et al.*, 2001]. It should be stressed that the Stokes vector A at the antenna level is not the Stokes vector S of the radiation from the surface. A and S are linked by a linear matrix operator which depends on both the full antenna patterns and the geometry of the observation setup [*Claassen and Fung*, 1974; *Ludwig*, 1973; *Waldteufel and Caudal*, 2002].

2.3. Science Requirements

[23] Any Earth observing system may be characterized by three basic performances: spatial resolution at ground level, sampling frequency, and accuracy on the retrieved parameters. For the purpose of optimization it is first necessary to assess how the scientific requirements impact these basic quantities.

2.3.1. Soil Moisture

[24] Spatial resolution is a driving factor for soil moisture, particularly with respect to hydrological science. As SMOS is a demonstrator and as there are currently no existing means of retrieving globally SM from space, it was recognized right at the beginning [*Kerr*, 1998] that ultimate needs in this respect, i.e., 1 to 20 km, would not be met by the mission. The goal was to achieve a resolution better than 50 km to be useful in models such as those currently run at the European Centre for Medium Range Weather Forecast (ECMWF) in Europe, or the National Centers for Environmental Prediction (NCEP) in the United States [*Jackson et al.*, 1999]. It was also necessary to define what was meant by resolution. The pixel size s is the equivalent diameter of the area where the directional power gain of the synthetic beam is larger than half its maximum value. In addition, since pixel shapes are close to ellipses with various orientations, their elongation e, i.e., the ratio of maximum to minimum sizes, is limited to values smaller than 1.5; this is meant to ensure that the pixel shape does not differ too much from a circle, in order to maximize the common area seen at different angles along the dwell lines.

[25] Concerning the temporal sampling frequency, it is necessary to be able to capture the main hydrologic events such as rain and dry-down episodes, which leads to a maximum acceptable time interval between two acquisitions of about 3 days. Indeed, numerical simulations for retrieving deep soil moisture from SM give the same temporal constraint [*Calvet et al.*, 1998]. It should be noted that the three-day revisit criterion applies to the 6 a.m. orbit only, as it is not sure to which extent it will be possible to correct the evening data for the diurnal

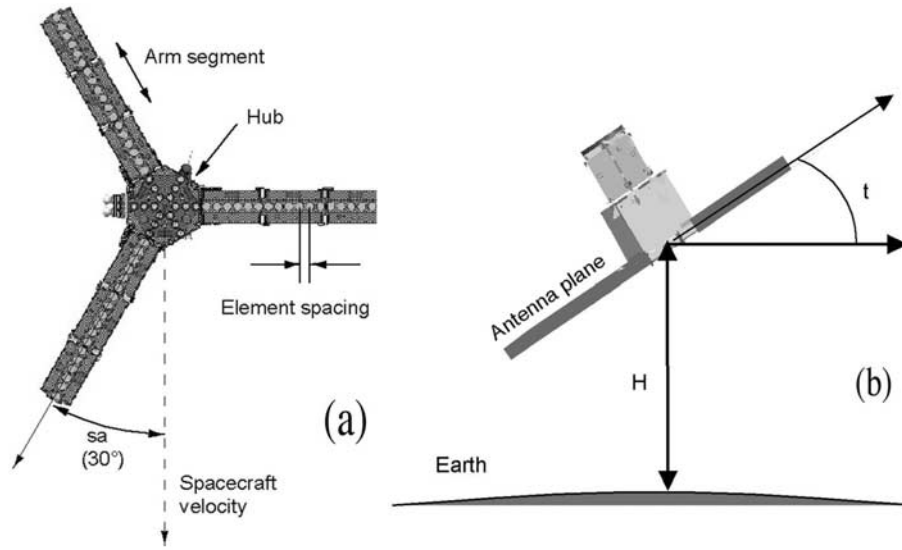

Figure 2. (a) Sketch of the Y-shaped interferometer design for the SMOS mission (courtesy of CASA-EADS, Spain). Shown are the central hub and the external arms consisting of several segments. A 30° steering angle has been selected. (b) Schematic side view of the spacecraft, showing the tilt angle. The solar panels have been omitted. See color version of this figure at back of this issue.

cycle. A sun-synchronous, 6 a.m. orbit was chosen so as to ensure global coverage, and to achieve the optimal trade off between (1) mission design requirements by maximizing the available solar power and minimizing perturbing factors linked to the ionosphere [*Le Vine and Abraham*, 2002], and (2) science objectives by minimizing the temperature and moisture vertical gradients [*Kerr et al.*, 2001].

[26] The accuracy required for SM measurements is taken to be 4% (volume, i.e., 0.04 m^3 m^{-3}). While this will most probably not be the case for OS, it is assumed here that most of errors on retrieved SM are random contributions that arise due to radiometric uncertainty.

[27] The temporal sampling constraint mentioned above translates readily into a swath requirement, which is most severe at the equator when only the ascending (or descending) orbit is considered. It is worth noting that the spatial resolution constraints will also result into swath limitations: as illustrated on Figure 1, both pixel size and elongation reach high values as the distance to the ground track becomes large. A similar point can be made for retrieval accuracy, as the dwell line lengths decrease away from the ground track, resulting into a decrease of the number of independent data samples available for the corresponding abscissas across the FOV. Therefore it will be possible to carry out the optimization process by selecting the configurations that provide the broadest overall swath compatible with science requirements, provided they are not detrimental to the swath's center measurements.

2.3.2. Ocean Salinity

[28] Since oceanic surfaces are significantly more homogeneous than land surfaces, spatiotemporal resolution is less of a driving factor. Conversely accuracy is a major issue. According to the Global Ocean Data Assimilation Experiment (GODAE) requirements, the optimized accuracy needed for ocean circulation applications is 0.1 PSS for a grid scale of 200 km every 10 days (see http://ioc.unesco.org/goos/Sydn/Sydn_a3.htm). Consequently, with respect to the mission optimization, spatiotemporal constraints for OS salinity retrievals are well within those for SM retrievals. However, the instantaneous swath of the measurement area will remain an important factor when assessing the number of independent data available for averaging.

3. Deriving the Optimal SMOS Configuration

3.1. Technical Constraints

[29] The SMOS instrument design, depicted on Figure 2a, is based on 3 coplanar arms consisting each of either two or three segments and attached to a central part (hub) where 3 elementary elements are aligned with each arm. The segments are made with either 6, 7 or 8

aligned elementary radiating elements. All in all, the number N of elements per arm is therefore only allowed a restricted set of 4 values $N_a \rightarrow N_d$: $N_a = 3 + 2 \times 8 = 19$, $N_b = 3 + 3 \times 6 = 21$, $N_c = 3 + 3 \times 7 = 24$, $N_d = 3 + 3 \times 8 = 27$. N_a had to be ruled out because the spatial resolution is found inadequate.

[30] Cost limits set to opportunity projects inexorably translate into payload limitations. The SMOS proposal included from the beginning the choice of the PROTEUS platform, which is adequate for mini satellite missions. The PROTEUS platform was developed by the Centre National d'Etudes Spatiales (CNES) and Alcatel. Space Industries. The platform architecture is generic. The spacecraft bus is roughly a 1 m cube and can accommodate a 300 kg payload requiring 400 W. Data is transmitted to the ground using an X band link [*Silvestrin et al.*, 2001].

[31] The main payload limitation when considering compatibility with PROTEUS was found to concern the length of the arms, which impacts on payload mass and inertia. The platform is controlled by inertia wheels, which impose a limit on spacecraft inertia for orbit maneuvers and in particular recovery when the satellite has been put on safe hold mode. Overall, it was initially estimated that the arm length L could not extend much in excess of 4,5 m, considering the required lineic mass for the arm structure.

[32] The range allowed for the spacing ratio d is limited upward to 0.9, beyond which value the alias free zone becomes exceedingly small; downward, values lower than 0.8 are precluded due to coupling effects between adjacent antennas. Since coupling effects worsen when d decreases, highest possible values for d within this range are preferred.

[33] Considering again the number of elements per arm N, it is then found that the N_d case can only be considered for spacing ratios close to the 0.8 lower limit, for which $L \approx 4.62$ m.

[34] Regarding flight altitude, higher values are preferred on technical grounds, since they provide longer visibility periods for telemetry, better altitude stability with respect to atmospheric drag, and shorter duration of sun eclipses.

3.2. What is Meant by Optimization

[35] The purpose of optimization is to find the best trade-off between (1) technical constraints and (2) fulfillment of the scientific objectives of the mission, in terms of those mission/instrument parameters which have mixed and sometimes contradictory influences. Therefore the procedure chosen does not take into account parameters that have nonambiguous effects, such as for example the receiver noise figure. Similarly, parameters such as equator-crossing time are not considered, as it only involves accuracy issues, even though it is scientifically a relevant mission characteristic.

[36] As described in section 2, all three basic science requirements, i.e., resolution, revisit and accuracy, can be expressed in terms of maximum instrument swath. To clarify further, Table 1 depicts the influence of mission parameters on various swath-limiting factors. The five main mission parameters to be considered appear on Figures 2a and 2b. They are: (1) the flight altitude H; (2) the tilt angle t of the antenna plane with respect to the local horizontal plane; (3) the steer angle sa; sa = 0°/30°, depending whether one of the arms lies in the orbital plane or is perpendicular to it, respectively; (4) the number N of elements along each interferometer arm; and (5) the spacing ratio d.

[37] The arm length L is obviously a relevant parameter, since $L = (N + 0.5)\,\lambda\,d$, where the 0.5 contribution accounts for the radius of the central element. For the sake of clarity, L is included in Table 1 as an alternate possible choice, provided either N or d is derived from the above relationship. Note that N has to be an integer number.

[38] As shown in the table, the swath limits are sensitive to all 5 parameters with varying amplitude and signs. It should also be noted that the signs of variation given here refer to limited parameter ranges around a representative configuration. They are not always monotonous. As an example, if increasing the tilt angle around 30° broadens the accuracy-limited swath, choosing very high values will ultimately narrow it, since the radiometer becomes pointed toward deep sky.

[39] The apodization window is a multiplying function applied to the visibility samples provided by the interferometer, in order to reduce adverse effects induced by the limits of the available baseline domain. An important characteristic of the window function is its angular width β, considered here in the domain of reconstructed temperatures. This is a processing option rather than a ''physical'' mission parameter. Nevertheless, it deserves a mention in Table 1, due to its conflicting influences on the ground surface spatial resolution and retrieval accuracy. However, the impact of contamination through side lobes and the outer part of the main lobe is also an important factor in selecting the window. For optimization purposes, a particular apodization function has to be selected among many possibilities [*Anterrieu et al.*, 2003]. In what follows, we have used the (exact) Blackmann window, as it is expected to be close to an optimum in terms of protection against contamination in the vicinity of a target discontinuity line such as a coastline.

3.3. Steer Angle and Flight Altitude Options

[40] As described above, the steer angle **sa** defines the orientation of the arms with respect to the orbital plane. The sa = 0° option selected in the original proposal,

Table 1. Sensitivity of Swath Width to Configuration Parameters[a]

Main Mission Parameters	Range of Values	Swath Width			Boresight Radiometric Sensitivity		Element 3 dB Gain Span	Swath Width
		FOV Ambiguities (Aliases)	Spatial Resolution					Random Uncertainties
			Pixel Size, s	Elongation, e	F_B	Tsc		
Flight altitude H, km, increases	680 720 760	++	= –	++	=	= –	++	++
Tilt angle t, °, increases	25 30 35	++	= –	++	=	= –	++	++ (– – for high t values !)
Steer angle **sa**, °, (two values)	0° 30°	++	=	=			=	
Arm length **L,** m, increases (fixed spacing ratio)	3.70 4.00 4.30	=+	=+	=	=+	=	=	= –
Spacing ratio d increases (fixed arm length L)	.84 .86 .88	– –	=	=	= –	=+	– –	– –
Element number N increases (fixed spacing ratio d)	20 22 24	=+	++	=	++	=	=	= –
Spacing ratio d increases (fixed element number N)	.84 .86 .88	– –	++	=	=	= –	– –	– –
Window width β increases			– –			++		

[a]Trends of the three swath limits discussed in section 3.2 when the configuration parameters vary around a reference set of values, for a representative set of target characteristics (see Appendix A). Symbols (++, =+, =, = –, ––) stand for increase, slight increase, stability, slight decrease and decrease, respectively. Two options are shown for the variations of the interrelated (L, d, N) parameters. Note that the two geometrical limits (due to s & e) may have different or even opposite trends. While both alias and geometrical limits are computed independently, the accuracy-limited swath is influenced by them, as they restrict the dwell line length along the track. In addition, other factors bear upon the accuracy: the table shows the trends of the boresight radiometric sensitivity components when written $\Delta T_B = F_B$ (Tsys + Tsc), where Tsys is the noise temperature, Tsc is the scene temperature and the F_B factor includes parameters of the receiver, interferometer and apodization window. The directional radiometric sensitivity is further affected by the 3 dB gain span (also shown) covered at ground level by the element antenna.

shown on Figure 3a, was only found worthwhile considering for very low values of the d parameter. Otherwise, as illustrated by Figure 3b, the along track abscissa of corresponding alias limits does not match well those due to spatial resolution limits, which results in a reduced swath width. Hence the sa = 30° option, selected for Figure 1, is to be preferred.

[41] For a sun synchronous orbit, in order to achieve global coverage within a given number of days at the equator with morning passes only, the required swath is driven by the flight altitude. Figure 4 shows, as a function of H in the 600–850 km range and the swath width, the limits of areas corresponding to given revisit times (expressed in days) for ascending orbits. Ruling out altitudes lower than 600 km as they are unsatisfactory when considering the performances in terms of pixel elongation and alias limits, two fairly narrow triangle-shaped areas remain, which allow to meet the 3-day revisit time requirement, provided the swath is broader than an altitude dependent minimum value $S_m(H)$, always larger than about 920 km.

[42] It seems safer to retain, in both cases, the side of the triangular area for which the variation of S_m is mildest, so as to loosen constraints on altitude control. Then, as preliminary tests indicated that the maximum achievable swaths are around 1150 km, only two altitude range need be considered: $H_a \approx 675 \pm 10$ km and $H_b \approx 760 \pm 10$ km. Since performances other than the revisit time vary quite smoothly with altitude, it will be adequate to retain in a first step a H value close to the middle of each range, and to tune, if necessary, the effect of adjusting the altitude by a few km at a later stage.

4. Optimization for Land Surfaces

4.1. Double Revisit Time/Swath Constraint

[43] The basic rationale for SM retrievals is to use multi angular measurements to infer SM, optical thickness τ of vegetation cover and surface temperature T_S, assuming an auxiliary estimate is available for the latest. However, the swath limited by the accuracy requirement

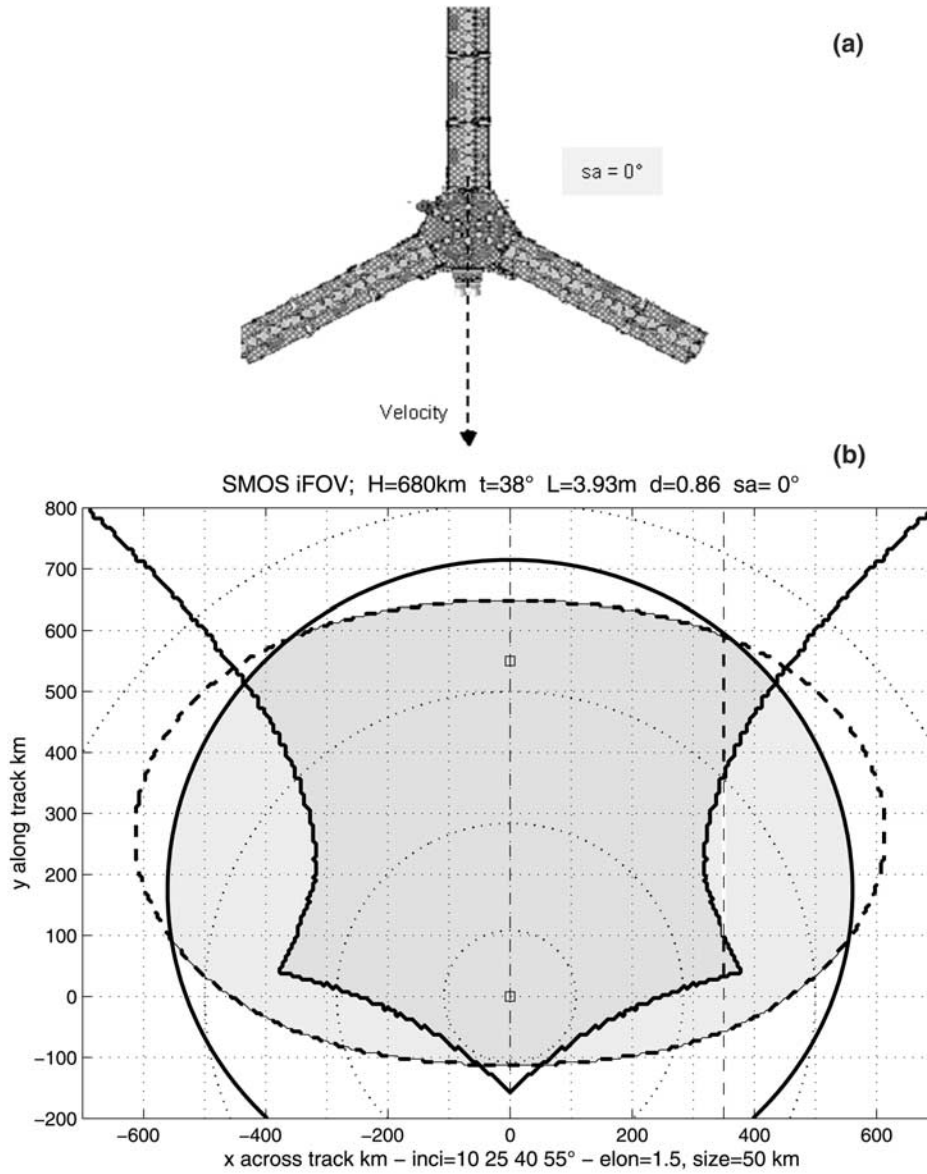

Figure 3. (a) Same as Figure 2a, for a 0° steering angle. (b) Same as Figure 1, for a 0° steering angle. For the same 350 km distance away from ground track as in Figure 1, the dwell line is much shorter and fragmented in two parts. See color version of this figure at back of this issue.

for SM is found to be strongly dependent upon whether a priori knowledge of τ is also available, since uncertainties on both retrieved parameters increase with decreasing dwell line length as it gets away from the ground track. For most tilt angles, this trend is enhanced by the transformation from the ground level reference frame to that of the antenna [*Waldteufel and Caudal*, 2002].

[44] To overcome this difficulty, and considering that the timescale of variations for τ is substantially higher than for soil moisture, a scheme has been suggested [*Wigneron et al.*, 2000]. This approach consists in using τ values, retrieved in the central part of the FOV on a previous orbit, as a priori information in order to improve the retrieval conditions for soil moisture in the outer parts of the FOV. The implication is that it becomes necessary to comply with 2 revisit time constraints: the nominal 3 day requirement stipulated above, and a requirement applied to a ''narrow swath,'' devoted to estimating simultaneously both SM and vegetation thickness without any a priori information on the latest; the ''narrow

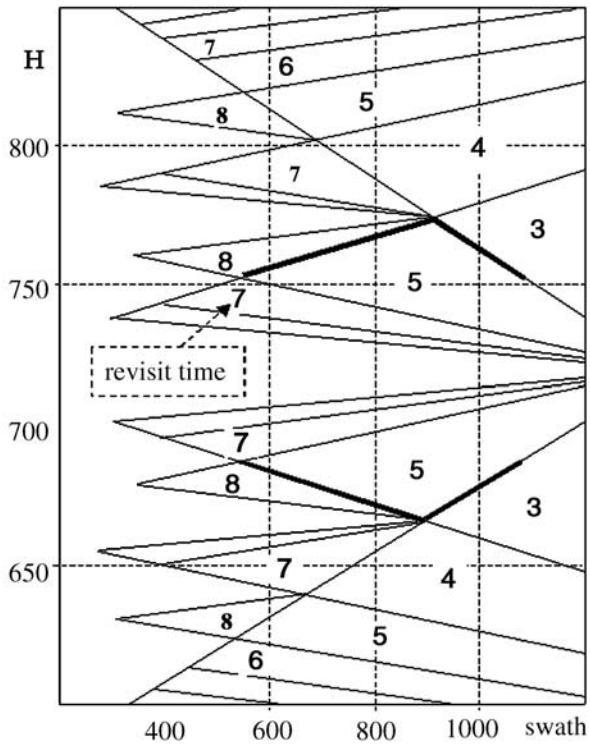

Figure 4. Revisit time at the equator for the morning (or evening) orbit, mapped as a function of flight altitude (vertical axis) and swath width (horizontal axis). The revisit time is indicated in days for zones delineated by solid lines. The minimum swath widths for 3 and 7 day revisit times, over the altitude ranges of interest for SMOS, are indicated by thick black linear segments.

swath" ought to be revisited at intervals at most equal to 7 days.

4.2. Implementation

[45] Two minimum required swath widths $S_{m3}(H)$, $S_{m7}(H)$, for both revisit times, approximated by tilted straight-line segments, are depicted on Figure 4. For both altitude ranges H_a and H_b under consideration, these lines express a set of 2 minimal swath widths to be achieved simultaneously at a given altitude.

[46] First, instrument characteristics and processing parameters are chosen (see Appendix A); next, for each mission configuration in the optimization domain, a couple (S_3, S_7) of swath values which meets the spatial resolution and accuracy requirements is obtained by simulating the retrieval; then the altitude H is tuned in order to find the maximum value ΔS for the average difference:

$$\Delta S = \max[0.5(S_3 + S_7 - S_{m3}(H) - S_{m7}(H))]. \quad (2)$$

The ΔS function thus provides the optimization criterion: the requirement is that ΔS should be positive.

4.3. Results

[47] Based on the previous sections, the optimization was performed by exploring the 0.8–0.9 domain for d, as well as the variation of the tilt angle t from nadir to 50°, for two representative altitudes, and 3 values $N_b = 21$, $N_c = 24$, $N_d = 27$ of the number of elements.

[48] Figure 5 shows maps of ΔS as a function of d and **t**, for the 6 combinations of altitude and element numbers to be considered.

[49] Significant parts of the maps depict strongly negative ΔS values, mostly for low tilt angles. This corresponds to cases where the "narrow swath" S_7 is very thin or even nonexistent, due to a too limited available range of incidence angles, leading to a poor sensitivity to vegetation optical thickness.

[50] Even with the help of Table 1, the overall picture is not easy to interpret, owing to the complexity of the feedback effects between configuration parameters. In addition, some optimum values are not available as they fall out of the technically allowed domain. For example, it may seem puzzling that for the lowest altitude the best performances are found for the intermediate N_c value. For the $N_b = 21$ case which corresponds to shorter arm lengths, the pixel size limit drives the optimum toward high d values, but then the loss of sensitivity away from boresight, due to the narrower element antenna gain pattern, becomes significant. For the higher N values, since the pixel size limit is no longer relevant, the optimum is driven toward low d values, taking advantage of a larger antenna gain on the FOV edges. However, when N reaches Nd = 27, the loss of boresight radiometric sensitivity, which is approximately proportional to N, overcomes this trend.

[51] The performances depicted by maps pertaining to the lower altitude are generally poorer. A likely reason for this is that both alias and elongation limits favor higher altitudes: see Table 1.

[52] The best performances are achieved for high N values. While increasing N has an adverse effect upon radiometric sensitivity [*Camps et al.*, 1998], there is some compensation at high tilt angles, in the range considered here for this parameter, because the sky contribution to the scene becomes larger, resulting in a cooler scene temperature and thus an improved radiometric sensitivity. The dwell lines are longest for low spacing ratio values, as it essentially removes the pixel size limit (see above).

[53] Even though this preliminary analysis shows the optimum number of elements to be either N_c or N_d, progresses in the technical analysis made these options unpractical as they induced instrument inertia to be too

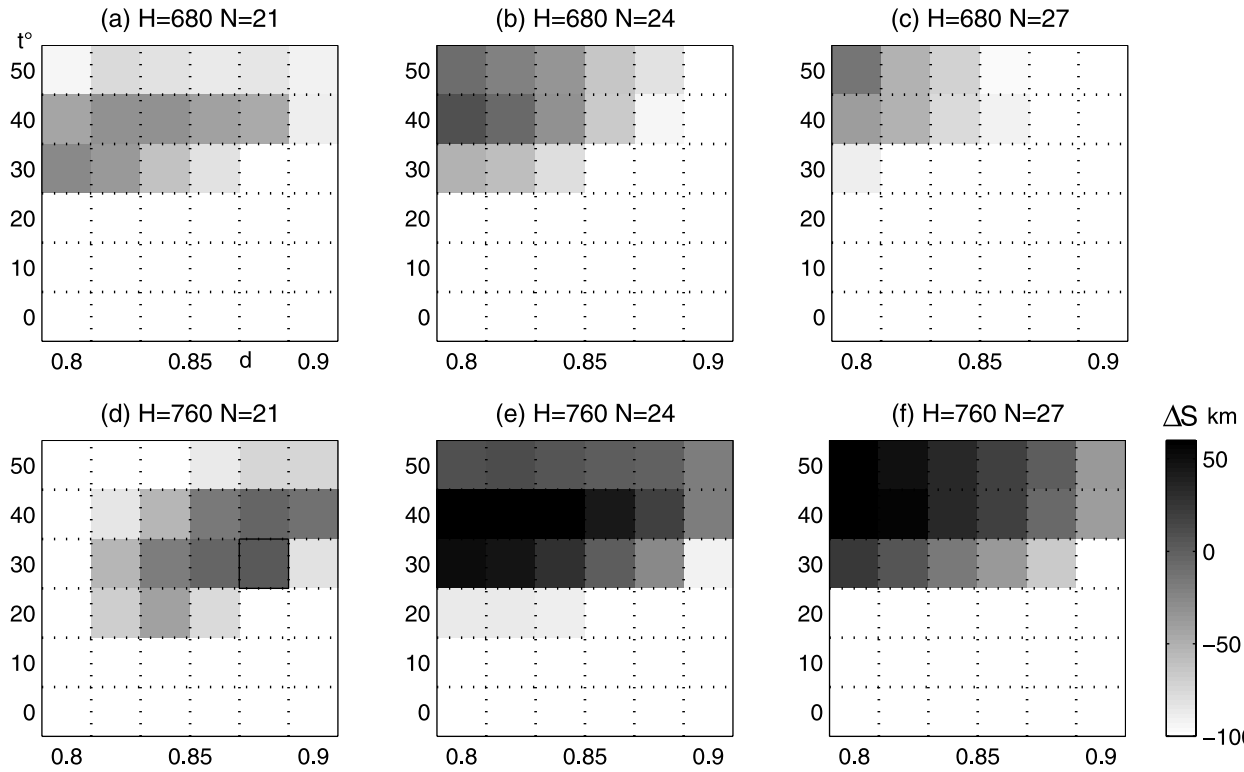

Figure 5. Land observation case; maps of the dual swath ΔS (K) criterion on a (d, t) grid. The maps (a)–(f) are shown for two altitudes and three values of the number N of elements. Grid steps are 0.02 for d and 10° for t. The optimal area selected on Figure 5d is indicated by a solid box.

high for the platform (see section 3.1 above). Consequently, so as to achieve a design with adequate margins for a phase A study, the configuration with $N = N_b = 21$ was preferred. For the high altitude range, there is a zone (see Figure 5d) where the ΔS criterion is just compliant. In that case the pixel size limit is operative, in such a way that the optimum is found for an intermediate tilt angle and a relatively high spacing ratio.

[54] A zoom of the map for this case (N = 21, 760 Km), shown on Figure 6, points to a well-defined ΔS maximum for $d \approx 0.875$, $t \approx 33°$, although another favorable area seems to exist for somewhat higher d and t values. The actual optimum altitude is seen to lie very near the original 760 km value; a further iteration was carried out and showed the impact of altitude differences to be negligible.

5. Ocean Measurements

5.1. Averaging Issues

[55] The goal of this section is to assess the impact of the mission configuration on OS retrievals where an averaging procedure is used. For this purpose, we first compute theoretical uncertainties σ_x over salinities retrieved for abscissas x across track. The x grid step is chosen smaller than any pixel size δ_x, in such a way that the T_B are over-sampled; hence, errors for adjacent x values are not independent.

[56] Next, a mean error $\langle\sigma_x\rangle$ over the FOV is computed for an average pixel size $\langle\delta_x\rangle$, i.e., the mean pixel size obtained over the FOV. Due to re-sampling, $\langle\delta_x\rangle$ and average variance of the error $\langle\sigma_x\rangle^2$ are the weighted means of δ_x and σ_x^2, respectively, the weights p_x being:

$$p_x = 1/\left(\sigma_x^2\delta_x\right). \tag{3}$$

In this formula, δ_x is the average pixel size along the dwell line at abscissa x. It should be noted that both factors in p_x decrease as x increases.

[57] For any configuration and corresponding FOV, it is then possible to derive the average uncertainty $\langle\sigma_x\rangle$ on an OS value retrieved from data with a spatial resolution $\langle\delta_x\rangle$:

$$\langle\sigma_x\rangle = \sqrt{\sum 1/\delta_x \sum 1/\left(\sigma_x^2\delta_x\right)}, \tag{4}$$

where the summation is done over the over-sampled pixels across track.

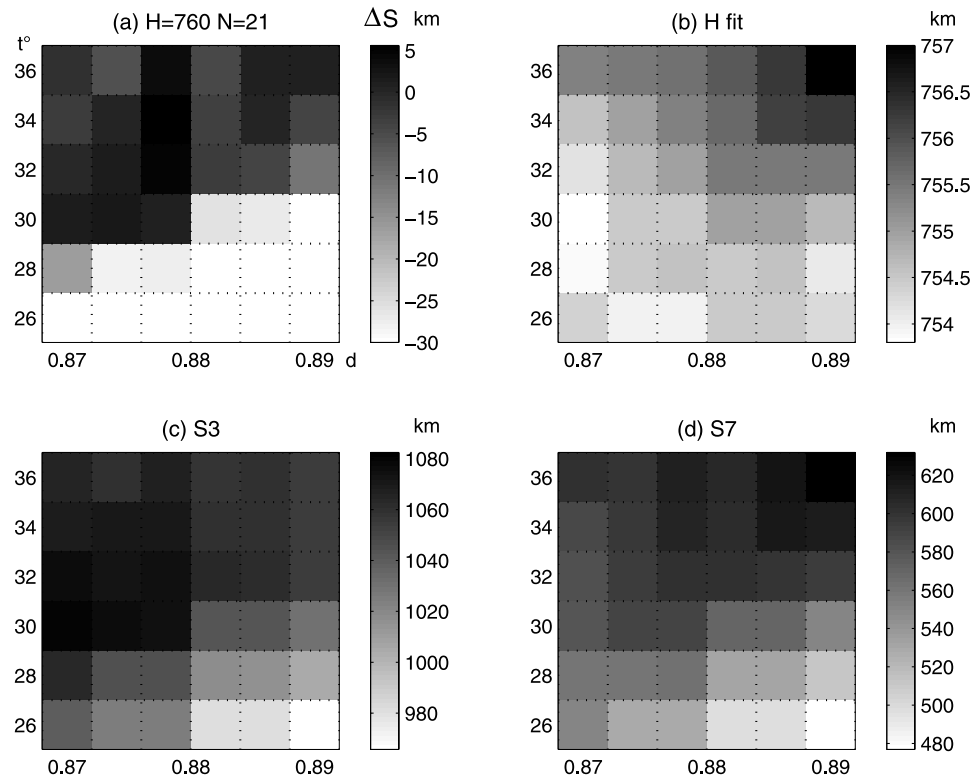

Figure 6. (a) Map of ΔS for H = 760 km, N = 21, over an expanded (d, t) grid centered on the optimal area delineated on Figure 5d. Steps are 0.004 for d and 2° for t. Lack of smoothness at small scales may be partly due to the choice of coarse FOV analysis grids, for the sake of computing time. Also shown are: (b) the exact altitude (km) for which the maximum ΔS value is found; (c) and (d): the actual swath widths for both 3 and 7 day revisit times (km).

[58] The following step is to derive an estimate σ_b of the OS retrieval error after averaging over an appropriate space-time domain.

[59] Using a statistical number of satellite passes, σ_b is derived from $\langle\sigma_x\rangle$. Assuming there are M_b independent retrieved OS values inside the spatiotemporal averaging area, we have:

$$\sigma_b = \frac{\langle\sigma_x\rangle}{\sqrt{M_b}}. \tag{5}$$

Let Δx, Δy, Δt be the sizes of the averaging area in space and time; used values are Δx = Δy = 200 km, Δt = 10 days. M_b can then be written:

$$M_b = m_1 m_2 m_3 / m_4, \tag{6}$$

where m_1 is the number of samples along x in the swath, $m_1 = \Delta x/\langle\delta_x\rangle$; m_2 is the number of samples along y, $m_2 = \Delta y/\delta y$; m_3/m_4, is the number of samples in time, where m_3 is the total orbital coverage, m_3 = number of orbits/day) x (Δt days), to be eventually multiplied by two if both ascending and descending passes are included; m_4 is the number of swaths SW necessary to cover a parallel circle, $m_4 = L_{LAT}/SW$; with L_{LAT} (equator) = 40000 km.

[60] While the along track spacing δy between independent data is proportional to the integration time, changing it is compensated by a change of $\langle\sigma_x\rangle$ due to the impact of the modified radiometric sensitivity. Note that data along y, even when over-sampled with respect to spatial resolution, are independent since they are obtained from different time intervals. The accumulation of retrieved estimates to be averaged is sketched on Figure 7 for the space domain.

[61] Typical values are: $m_1 \approx 5$ for an average $\langle\delta_x\rangle$ = 40 km; $m_2 \approx 10$ for a 20 km interval along track between successive integrations; $m_3 \approx 143$; $m_4 \approx 36$ at the equator, assuming a swath 1100 km wide. The resulting value for M_b is around 200 and therefore σ_b is found smaller than $\langle\delta_x\rangle$ by a factor of about 14.

[62] Over 10 days, a given 200 km wide area near the equator will be seen about 4 times by the satellite, as m3/m4 ≈ 4; consequently, the averaging process will not include an exploration of the whole swath width. For this

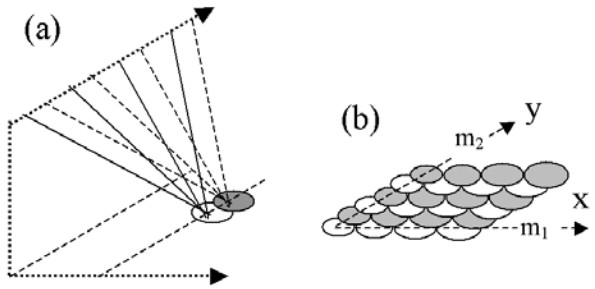

Figure 7. (a) Outline of the building of multi angular observations as the spacecraft moves ahead. (b) Outline of the averaging process in a space domain. References to the m_1 and m_2 factors in the text, equation (6), are indicated. Note that apparent overlapping occurs along the *y* axis; across the FOV, on the other hand, unequally sized pixels are juxtaposed.

reason, the estimate given here is only valid in a statistical sense. Actual simulations of the flight are necessary to assess the amplitude of variations around this estimate.

5.2. Variation of σ_b With Configuration Parameters

[63] Figure 8f shows as a final result the uncertainty σ_b over space-time averaged retrieved OS, for the configuration domain selected for land surfaces (see Figure 5). The main result is that variations of σ_b are smooth and rather small, around an average value of about 0.05 PSS. The highest altitude range has marginally better performances with respect to the lower one (not shown).

[64] Maps of various quantities, which contribute to explain the trends of the resulting uncertainty, are also depicted on Figure 8. It is worth noting that in Figure 8a, the variation of radiometric sensitivity is mainly due to increased deep sky cold contribution when the tilt angle increases. In Figure 8b, the FOV in terms of solid angle hemispheric coverage, taken as an overall indicator of the length of dwell lines, becomes higher for small spacing

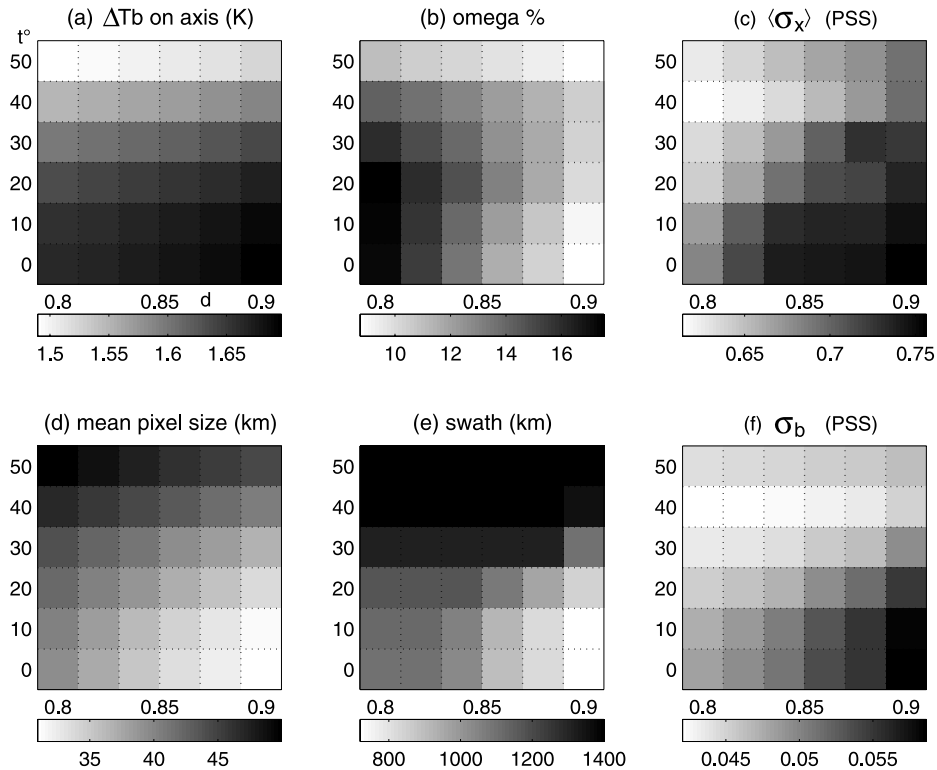

Figure 8. Ocean observation case: for the same (N, H) configuration as the one selected for land surfaces (Figure 5), on the same (d, t) grid, are shown maps of: (a) the boresight radiometric sensitivity (K); (b) the fraction of solid angle for which ocean surface is seen by the interferometer (in percent); (c) the average standard deviation $\langle\sigma_x\rangle$ of OS over the FOV (PSS); (d) the mean pixel size (km); (e) the swath (km); (f) the standard deviation σ_b on space/time averaged OS (PSS).

ratios. And in Figure 8c, the resulting $\langle\sigma_x\rangle$ uncertainty is found lowest near the (t = 40°, d = 0.8) grid square. Averaging over a space-time domain does not change this trend, since the mean resolution (4d) and swath (4e), which appear as a ratio in the M_b formula, exhibit similar variations across the exploration grid.

[65] Consequently, by selecting the configuration optimal for land surface observations, the loss of accuracy for sea observations is not larger than 10% with respect to the possible optimum, which is in the uncertainty domain.

5.3. Ancillary Parameters: Surface Temperature and Wind Speed

[66] It is well known [*Klein and Swift*, 1977] that the sensitivity of T_B to OS decreases with sea surface temperature (SST). The consequences of this variation over the retrieval performance across the SMOS FOV are significant, as illustrated by Figure 9a, which depicts σ_x as a function of x and the SST. On the other hand, the dependence of T_B on the SST is weak [*Yueh et al.*, 2001], and the relative contribution of SST uncertainties to OS retrieval uncertainties is found negligible when compared to those arising from radiometric uncertainty and errors on a priori wind estimates.

[67] We face indeed an opposite situation for the wind speed U. While the sensitivity $\delta(T_B)/\delta(OS)$ is not strongly dependent upon wind values, the uncertainty on U is a significant contributor to $\langle\sigma_x\rangle$. As illustrated by Figure 9b, from a case where U is perfectly known to a case where no a priori knowledge of U is available, $\langle\sigma_x\rangle$ varies by a factor of about 3. Therefore it seems worthwhile attempting to obtain accurate a priori estimates of wind speed.

[68] However, such a priori estimates might be biased, for example due to deficiencies of the emissivity model. As shown in Figure 9b, uncertainties σ_U stipulated for a priori wind estimates should be significantly larger than potential wind biases, if one wants to avoid the propagation of such biases in OS retrieved values.

[69] Another limiting factor is that ancillary wind data cannot be expected to be fully independent, at least spatially, whereas independence would be required in the averaging process described above. The situation is then equivalent to having independent a priori wind estimates with larger σ_U values. For this reason, the numerical results given above for σ_b may be optimistic by several tens of percent. Corrected results would, however, still comply with the accuracy requirements for OS, as far as the random contribution is concerned.

6. Summary and Concluding Remarks

[70] The goal of this paper is to describe the optimization approach taken for the SMOS mission configuration. The rationale was to find the mission configuration satisfying the science requirements and compatible with a mini satellite. For this, the needs in terms of geophysical parameter retrievals were translated into instrument configuration for the specific case of a 2-D interferometer. Strictly speaking, optimization is not mandatory: what one needs to know is the domain of configuration parameters where these requirements are met. However, it turns out that this domain is quite restricted indeed, since even the optimal configuration does not yield significant margins.

[71] The parameters considered were altitude, tilt angle and orientation (steer) angle of the interferometer, number of elements per arm and spacing between elements, The optimization was carried out for the surface variable giving the most stringent criteria (SM) and then validated for the other (OS). Since external, technical constraints were introduced, the risk was high to obtain the best performances on the edge of the allowed domain.

[72] For one major mission parameter, the number of interferometer elements par arm, the selection was indeed imposed by technical constraints which set mass and inertia limits. Concerning both the interferometer steer angle and the flight altitude, the choice was fortunately restricted to a binary option Then, in the remaining tilt angle/spacing ratio domain, a well-defined optimum was actually found inside the allowed grid for the case of land surface observations. The optimized configuration is summarized as follows:

[73] N = 21; sa = 30°; H ≈ 755 km; t ≈ 33°; d ≈ 0.875. Even though efforts were implemented to define the best configuration in a logical way, several weaknesses must be acknowledged.

1. The results are somewhat dependent upon the target parameters selected (see Appendix A).

For land surface these have been chosen rather severely (high vegetation water content, low soil moisture). For more realistic and favourable cases in terms of retrieval [*Wigneron et al.*, 2000], additional margins will appear. On the other hand, for cases with uniform, very thick vegetation cover such as forested areas, the accuracy requirements will not be met everywhere. Note that the accuracy threshold for thickness τ within the narrow swath has a significant influence; the results might be improved by tuning this parameter according to specific scene features.

For ocean measurements, the influence of SST has been described over the SMOS swath. When averaging on space and time, the increased orbital coverage for colder seas is expected to compensate the loss in sensitivity to salinity. Overall, this has no influence upon selecting the optimal configuration.

2. The optimization has been carried out considering only random retrieval uncertainties, which originate from the radiometric sensitivity. This leaves asides errors due to both imperfect knowledge of the instrument (biases,

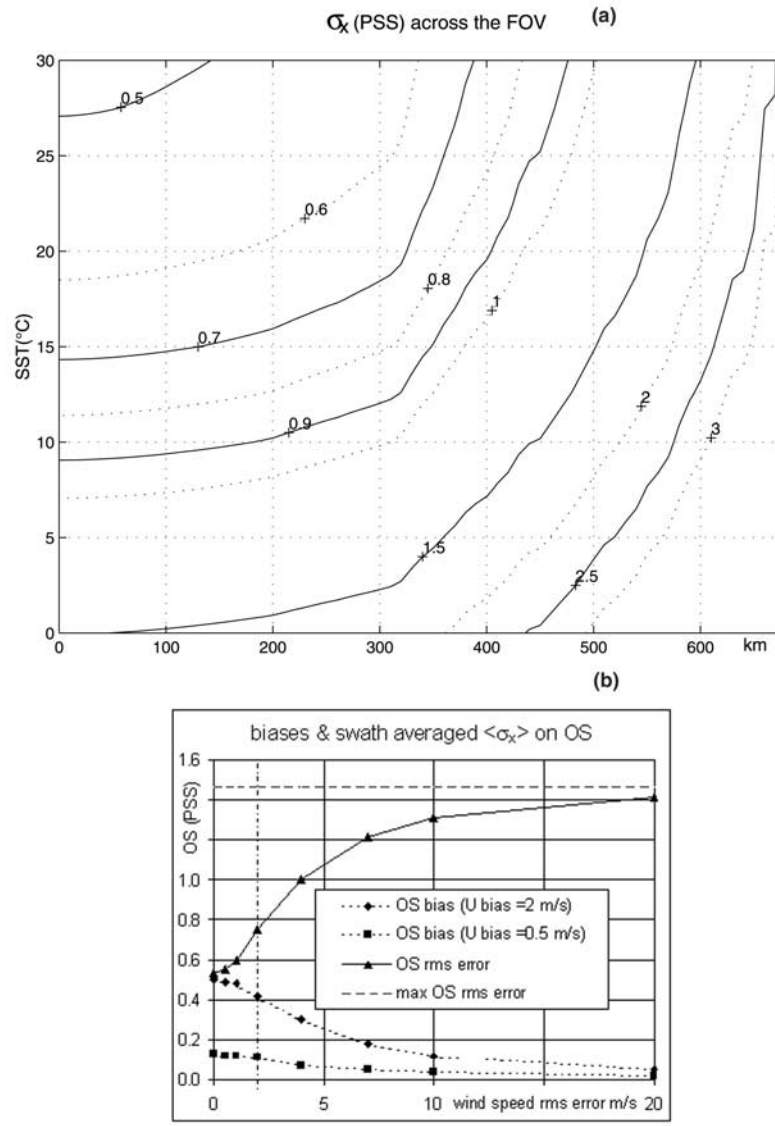

Figure 9. (a) SSS error as a function of SST (U RMS error σ_U = 2 m/s; SST RMS error σ_{SST} = 1 K), from the center of the swath to 680 km. (b) Mean OS uncertainty $\langle\sigma_x\rangle$ across the FOV as a function of the a priori uncertainty σ_U over the wind speed; the 2 ms^{-1} value, indicated by a vertical line, was used in the optimization study. Also shown are the resulting OS biases for two assumed biases over a priori U estimates, as a function of σ_U.

calibration errors), and to the variable pixel sizes and shapes, especially when looking at inhomogeneous targets; in addition, no account has be taken of possible deficiencies in the forward models. There is, however, no obvious reason to suggest that such errors should be relevant for the optimization.

[74] Although science requirements have been expressed in terms of simple, strict inequalities, a more sophisticated assessment of performances might introduce a variety of shades between binary compliance figures. For example the measurement accuracy depends on the spatial structure and content of the scene; a time sampling criterion might involve the fractional latitude coverage, and so on. It is expected that the optimum choice reached here will not be too far away from what would be obtained when considering statistical/climatological requirements, which undoubtedly are difficult to formulate.

[75] The method described in this paper should present some generic interest: estimating the atmospheric precipitating water content at centimetric microwave fre-

quencies offers an example of future possible applications of synthetic aperture radiometry in remote sensing.

Appendix A: Optimization Scheme and Instrument Modeling

[76] This section summarizes: processing options retained in the present work and technical information about the instrument model.

A1. Optimization

[77] In order to minimize the cost function (equation (1)), the retrieval uses a generalized least squares iteration method [*Marquardt*, 1963]. In the present application the algorithm reduces to a pure least squares computation, since it is only used (with exact initial values) in order to compute random uncertainties.

[78] The vector $[\sigma_i^2]$ of variances on retrieved parameters p_i is given by:

$$\left[\sigma_i^2\right] = \left[Q^t\ S^{-1}\ Q\right]^{-1}, \qquad \text{(A1)}$$

where S is the covariance matrix for data and a priori parameters, and Q is the derivative matrix. When retrieving at the antenna level, data are uncorrelated and the S matrix only consists of diagonal terms σ_m^2 and σ_0^2. The derivative matrix Q is rectangular with size (M + I) × I, where M is the number of data and I the total number of floating parameters. In order to build Q, the M × I matrix of derivatives of the model with respect to parameters is completed by a I-sized unity matrix

[79] Over land surfaces, emissivities and brightness temperatures T_B are computed according to the $\tau - \omega$ model [*Kerr and Njoku*, 1990]. Representative values were fixed for soil structure and roughness parameters. The main target properties are: SM = 10%; τ = 0.455 (3.5 kg m^{-2}); T_S = 293 K. An a priori uncertainty σ_{TS} = 2 K is assumed on T_S. Concerning the vegetation optical thickness, it is requested that the ''narrow swath'' data provide an estimate with a 0.065 uncertainty, that is: first no constraint on τ for the narrow swath, then σ_τ = 0.065 (≈ 0.5 kg/m2) for the nominal swath.

[80] Over the ocean, emissivities and T_B are computed according to the model established by *Klein and Swift* [1977]. The sea state effects are accounted for according to the model of *Yueh* [1997]. The chosen target properties are: OS = 35 (PSS); SST = 293 K; U = 10 m s^{-1}, with a priori uncertainties: σ_U = 2 m s^{-1}, σ_{SST} = 1 K.

A2. Instrument Model

[81] For the interferometric element, cup dipole theoretical full patterns were supplied by CNES. The boresight gain is assumed to be equal to 8.7 dB for a diameter, assumed equal to element spacing, of 18.7 cm (d = 0.89), in agreement with former MIRAS studies, and thereof proportional to d^2.

[82] The boresight radiometric sensitivity was computed according to *Camps et al.* [1998]. The assumed system noise temperature is 180 K; the scene temperature is computed allowing a 3.5 K average sky radiative temperature.

[83] The assumed receiving bandwidth is 19 MHz. The effective integration time is computed as: $\delta y/(v_0 \times 2 \times 1.81)$, where δy (km) is the integration length along the track, v_0 is the ground level satellite velocity ($v_0 \approx 6.7$ km s^{-1}); the factor 2 comes from commuting single receivers between both polarizations; the 1.81 factor is due to combined loss due to 2-bits correlation and gain through over-sampling in time.

[84] A 0.452 factor corresponding to the Blackmann window is used in the radiometric sensitivity equation, as well as a 0.82 reduction coefficient due to redundant visibility samples.

[85] Angular widths for the apodization window and the margin taken with respect to alias limits are 0.72 λ/L and 0.8 λ/L respectively.

[86] **Acknowledgments.** This work was supported by the Centre National d'Etudes Spatiales (CNES) and the Centre National de la Recherche Scientifique (CNRS). We are grateful to CNES for supplying simulated antenna patterns and revisit time data; to Jean-Pierre Wigneron and Emmanuel Dinnat for help with emissivity models; to Eric Anterrieu for assessment of apodization window and redundancy effects; to Nicolas Martin for computation support. ESA supported the 2-D interferometer studies within the MIRAS pilot development project.

References

Anterrieu, E., P. Waldteufel, and A. Lannes, Apodization functions for 2D hexagonally sampled synthetic aperture imaging radiometers, *IEEE Trans. Geosci. Remote*, 41, doi:TGRS-00158-2001, in press, 2003.

Calvet, J.-C., J. Noilhan, and P. Bessemoulin, Retrieving the root-zone soil moisture from surface soil moisture or temperature estimates: a feasibility study based on field measurements, *J. Appl. Meteorol.*, *37*, 371–386, 1998.

Camps, A., I. Corbella, J. Bará, and F. Torres, Radiometric sensitivity computation in aperture synthesis interferometric radiometer, *IEEE Trans. Antennas Propag.*, *36*(2), 680–685, 1998.

Chanzy, A., T. J. Schmugge, J. C. Calvet, Y. Kerr, P. VanOevelen, O. Grosjean, and J. R. Wang, Airborne microwave radiometry on a semi-arid area during HAPEX-Sahel, *J. Hydrol.*, *188–189*, 285–309, 1997.

Claassen, J. P., and A. K. Fung, The recovery of polarized apparent temperature distributions of flat scenes from antenna temperature measurements, *IEEE Trans. Antennas Propag.*, *AP-22*, 433–442, 1974.

Fischman, M. A., A. W. England, and C. S. Ruf, How digital correlation affects the fringe washing function in L band aperture synthesis radiometry, *IEEE Trans. Geosci. Remote Sens.*, *40*(3), 671–679, 2002.

Global Energy and Water Cycle Experiment/Biospheric Aspects of the Hydrological Cycle (GEXEW/BAHC), International workshop on soil moisture monitoring, analysis and prediction for hydrometeorological and hydroclimatological applications, *IGPO Publ. Ser. 35, Workshop Summary Rep.*, Univ. of Okla., Tulsa, 2000.

Jackson, T. J., and the Soil Moisture Mission Working Group, Report on Soil Moisture Mission Workshop, NASA, Washington, D. C., 2002.

Jackson, T. J., D. M. LeVine, C. T. Swift, T. J. Schmugge, and F. R. Schiebe, Large area mapping of soil moisture using the ESTAR passive microwave radiometer in Washita'92, *Remote Sens. Environ*, *53*, 27–37, 1995.

Jackson, T. J., et al., Soil Moisture Research Mission (EX-4), NASA Post-2002 Land Surface Hydrology Mission, *Workshop Rep.*, 26 pp., NASA, Washington, D. C., 1999.

Kerr, Y. H., The SMOS mission: MIRAS on RAMSES, A proposal to the call for Earth Explorer Opportunity Mission, Cen. d'Etud. Spatiales de la Biosphere, Toulouse, France, 1998.

Kerr, Y. H., and E. G. Njoku, A semiempirical model for interpreting microwave emission from semiarid land surfaces as seen from space, *IEEE Trans. Geosci. Remote Sens.*, *28*(3), 384–393, 1990.

Kerr, Y. H., J. Font, P. Waldteufel, A. Camps, J. Bará, I. Corbella, F. Torres, N. Duffo, M. Vallossera, and G. Caudal, Next generation radiometers: SMOS A dual pol L-band 2D aperture synthesis radiometer, paper presented at 2000 IEEE Aerospace Conference, Big Sky, Mo., 18–25 March, Inst. of Electr. and Electron. Eng., Aerosp. and Electon. Sys. Soc., New York, 2000.

Kerr, Y. H., P. Waldteufel, J.-P. Wigneron, J.-M. Martinuzzi, J. Font, and M. Berger, Soil moisture retrieval from space: The Soil Moisture and Ocean Salinity (SMOS) mission, *IEEE Trans. Geosci. Remote Sens.*, *39*(8), 1729–1735, 2001.

Klein, L. A., and C. T. Swift, An improved model for the dielectric constant of sea water at microwave frequencies, *IEEE Trans. Antennas Propag.*, *AP-25*, 104–111, 1977.

Lagerloef, G. S. E., C. T. Swift, and D. M. LeVine, Sea surface salinity: The next remote sensing challenge, *Oceanography*, *8*(44), 44–50, 1995.

Le Vine, D. M., and S. Abraham, The effect of the ionosphere on remote sensing of sea surface salinity from space: Absorption and emission at L band, *IEEE Trans. Geosci. Remote Sens.*, *40*(4), 771–782, 2002.

Ludwig, A. C., The definition of cross polarization, *IEEE Trans. Antennas Propag.*, *AP-21*, 116–119, 1973.

Marquardt, D. W., An algorithm for least-squares estimation of non-linear parameters, *SIAM, J. Appl. Math.*, *11*(2), 431–441, 1963.

Martin-Neira, M., and Q. Garcia, Pol Switching: Switching scheme for single channel polarimetric aperture synthesis radiometers, *ESTEC Working Pap. 2062-2*, 23 pp., Eur. Space Ag., Eur. Space Res. and Technol. Cent., Noordwijk, Netherlands, 1999.

Martin-Neira, M., A. Martin-Polegre, and S. Ribo, Introduction to two-dimensional aperture synthesis microwave radiometry for earth observation: Polarimetric formulation of the visibility function, *Intern. ESTEC Working Pap. 2130*, Eur. Space Ag., Eur. Space Res. and Technol. Cent., Noordwijk, Netherlands, 2001.

Schmugge, T. J., Applications of passive microwave observations of surface soil moisture, *J. Hydrol.*, *212–213*, 188–197, 1998.

Schmugge, T. J., and T. J. Jackson, Mapping soil moisture with microwave radiometers, *Meteorol. Atmos. Phys.*, *54*, 213–223, 1994.

Silvestrin, P., M. Berger, Y. H. Kerr, and J. Font, ESA's Second Earth Explorer Opportunity Mission: The Soil Moisture and Ocean Salinity Mission-SMOS, *IEEE Geosci. Remote Sens. Newslett.*, *118*, 11–14, 2001.

Swift, C. T., and R. E. McIntosh, Considerations for microwave remote sensing of ocean surface salinity, *IEEE Trans. Geosci. Remote Sens.*, *GE21*, 480–490, 1983.

Waldteufel, P., and G. Caudal, Off-axis radiometric measurements: Application to interferometric antenna designs, *IEEE Trans. Geosci. Remote Sens.*, *40*(6), 1435–1439, 2002.

Waldteufel, P., E. Anterrieu, J. M. Goutoule, and Y. H. Kerr, Field of view characteristics of a 2-D interferometric antenna, as illustrated by the MIRAS/SMOS L-band concept, in *Microwave Radiometry and Remote Sensing of the Earth's Surface and Atmosphere*, edited by P. Pampaloni and S. Paloscia, pp. 477–483, VSP, Zeist, Netherlands, 2000.

Wigneron, J. P., P. Ferrazzoli, J. C. Calvet, Y. Kerr, and P. Bertuzzi, A parametric study on passive and active microwave observations over a soybean crop, *IEEE Trans. Geosci. Remote Sens.*, *37*(6), 2728–2733, 1999.

Wigneron, J.-P., P. Waldteufel, A. Chanzy, J. C. Calvet, and Y. Kerr, Two-D microwave interferometer retrieval capabilities of over land surfaces (SMOS mission), *Remote Sens. Environ.*, *73*(3), 270–282, 2000.

Wilson, W. J., S. H. Yueh, J. Dinardo, S. L. Chazanoff, A. Kitiyakara, and F. K. Li, Passive active L and S band (PALS) microwave sensor for salinity and soil moisture measurements, *IEEE Trans. Geosci. Remote Sens.*, *39*(5), 1039–1047, 2001.

Yueh, S. H., Modeling of wind direction signals in polarimetric sea surface brightness temperatures, *IEEE Trans. Geosci. Remote Sens.*, *35*, 1400–1417, 1997.

Yueh, S. H., R. West, W. J. Wilson, K. L. Fuk, and E. G. Njoku, Error sources and feasibility for microwave remote sensing of ocean surface salinity, *IEEE Trans. Geosci. Remote Sens.*, *39*(5), 1049–1060, 2001.

J. Boutin, LODYC UPMC, Case 100, Tour 15 2e etage 4 Place Jussieu, 75252 Paris cedex 05, France. (jacqueline.Boutin@lodyc.jussieu.fr)

Y. Kerr, CESBIO, 18 Avenue du Colonel Roche 31, Toulouse, France. (yann.kerr@cesbio.cnes.fr)

P. Waldteufel, IPSL/SA, B.P.3, F-91371 Verrières le Buisson Cedex, France. (philippe.waldteufel@aerov.jussieu.fr)

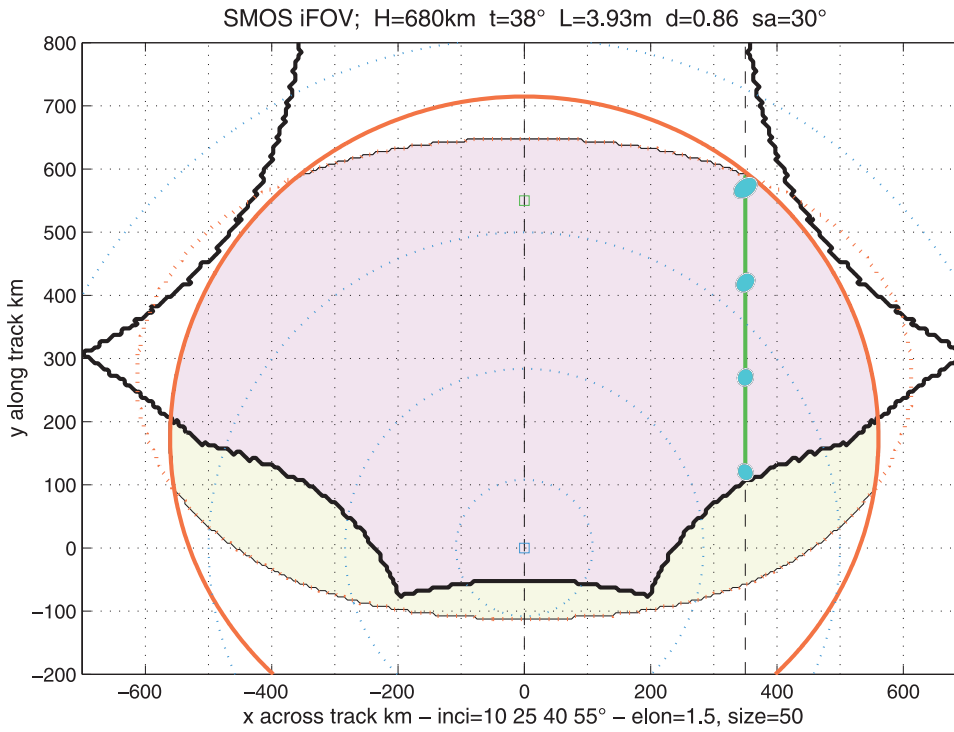

Figure 1. Example of the SMOS instantaneous FOV, when mapped on a geographical grid on Earth surface. The diagram is symmetrical with respect to the satellite track. Shown are the boundaries of the available zone for reconstructed brightness temperatures (thick black). Most of them are parts of ellipses, which correspond to replicated contours of Earth's horizon. Far on each side, straight-line segments indicate boundaries of the reconstruction zone. Also shown are spatial resolution limits (thick red line for pixel equivalent diameter s; thin red line for elongation e), contours of equal incidence angle (dotted blue; values 10, 25, 40, 55°), subsatellite point and intersection of antenna axis with Earth (squares), and a particular dwell line (green), 350 km away from ground track, along which samples of pixels are displayed.

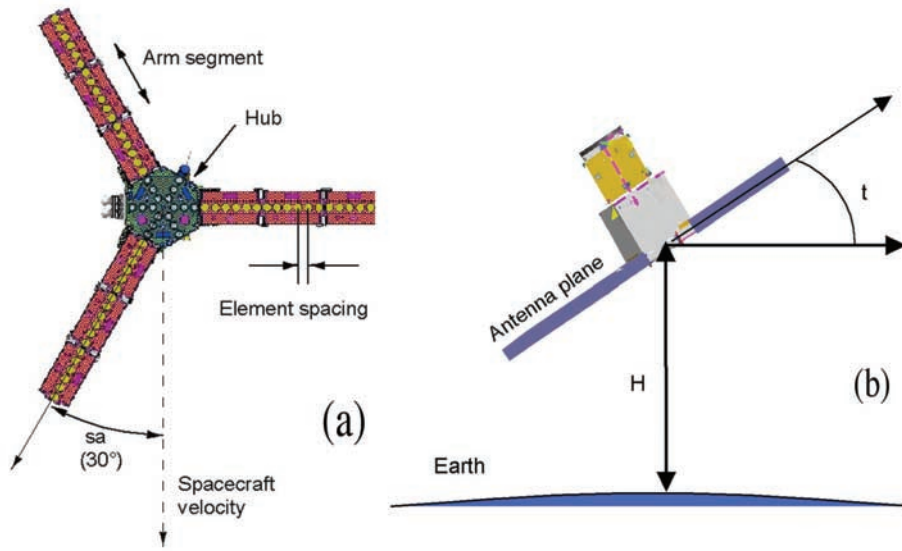

Figure 2. (a) Sketch of the Y-shaped interferometer design for the SMOS mission (courtesy of CASA-EADS, Spain). Shown are the central hub and the external arms consisting of several segments. A 30° steering angle has been selected. (b) Schematic side view of the spacecraft, showing the tilt angle. The solar panels have been omitted.

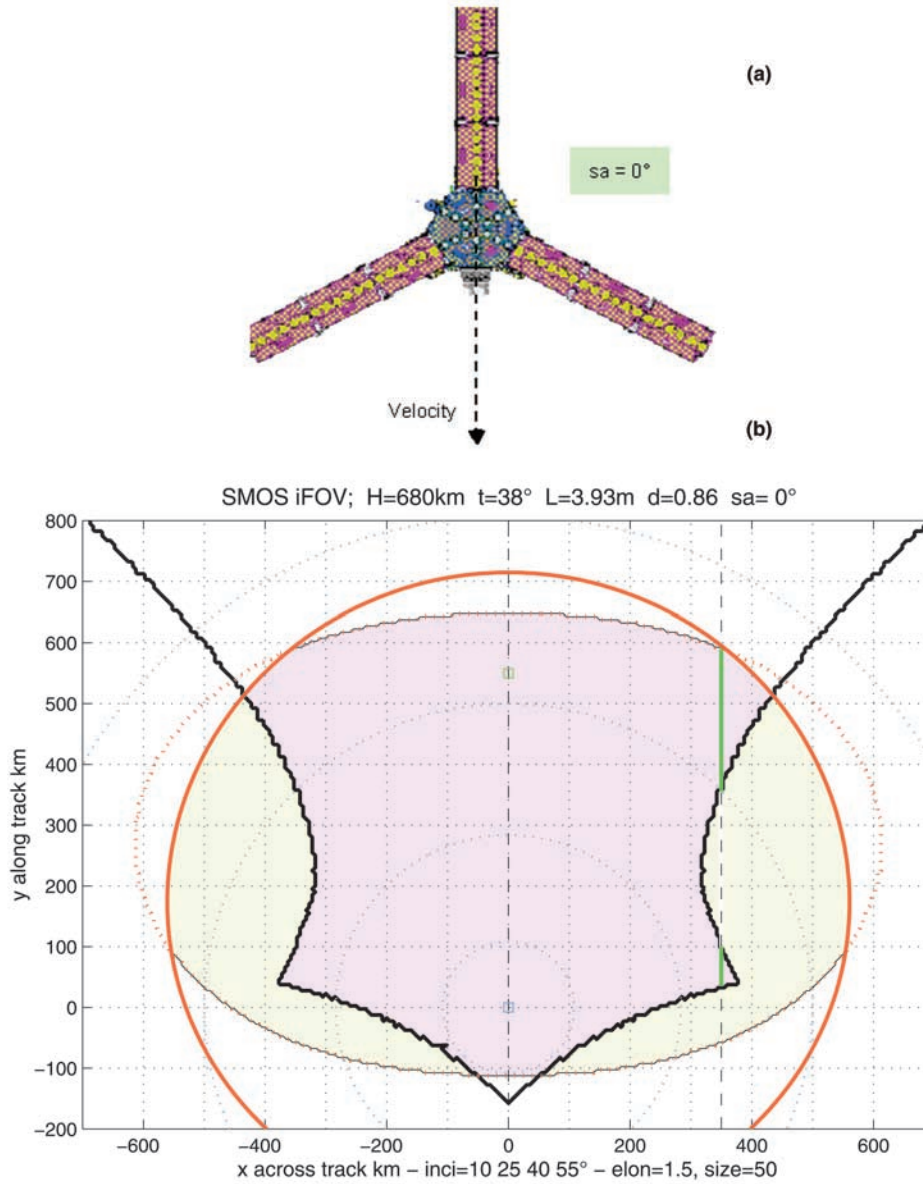

Figure 3. (a) Same as Figure 2a, for a 0° steering angle. (b) Same as Figure 1, for a 0° steering angle. For the same 350 km distance away from ground track as in Figure 1, the dwell line is much shorter and fragmented in two parts.